UC Berkeley

UC Berkeley Previously Published Works

Title

Longitudinal atlas for normative human brain development and aging over the lifespan using quantitative susceptibility mapping

Permalink

https://escholarship.org/uc/item/6vv9z971

Authors

Zhang, Yuyao
Wei, Hongjiang
Cronin, Matthew J
et al.

Publication Date

2018-05-01

DOI

10.1016/j.neuroimage.2018.01.008

Peer reviewed

Longitudinal Atlas for Normative Human Brain Development and Aging over the Lifespan using Quantitative Susceptibility Mapping

Yuyao Zhang[1,a], **Hongjiang Wei**[1,a], **Matthew J. Cronin**[1], **Naying He**[2], **Fuhua Yan**[2], and **Chunlei Liu**[1,3,*]

[1]Electrical Engineering and Computer Science, University of California at Berkeley, CA, USA

[2]Department of Radiology, Ruijin Hospital, Shanghai Jiaotong University School of Medicine, Shanghai, China

[3]Helen Wills Neuroscience Institute, University of California at Berkeley, CA, USA

Abstract

Longitudinal brain atlases play an important role in the study of human brain development and cognition. Existing atlases are mainly based on anatomical features derived from T1- and T2-weighted MRI. A 4D developmental quantitative susceptibility mapping (QSM) atlas may facilitate the estimation of age-related iron changes in deep gray matter nuclei and myelin changes in white matter. To this end, group-wise co-registered QSM templates were generated over various age intervals from age 1 – 83 years old. Registration was achieved by combining both T1-weighted and QSM images. Based on the proposed template, we created an accurate deep gray matter nuclei parcellation map (DGM map). Notably, we segmented thalamus into 5 sub-regions, i.e. the anterior nuclei, the median nuclei, the lateral nuclei, the pulvinar and the internal medullary lamina. Furthermore, we built a "whole brain QSM parcellation map" by combining existing cortical parcellation and white-matter atlases with the proposed DGM map. Based on the proposed QSM atlas, the segmentation accuracy of iron-rich nuclei using QSM is significantly improved, especially for children and adolescent subjects. The age-related progression of magnetic susceptibility in each of the deep gray matter nuclei, the hippocampus, and the amygdala was estimated. Our automated atlas-based analysis provided a systematic confirmation of previous findings on susceptibility progression with age resulting from manual ROI drawings in deep gray matter nuclei. The susceptibility development in the hippocampus and the amygdala follow an iron accumulation model; while in the thalamus sub-regions, the susceptibility development exhibits a variety of trends. It is envisioned that the newly developed 4D QSM atlas will serve as a template for studying brain iron deposition and myelination/demyelination in both normal aging and various brain diseases.

*Corresponding author: Chunlei Liu, PhD, Electrical Engineering and Computer Science, University of California at Berkeley, 505 Cory Hall, MC #1770, Berkeley, CA 94720, chunlei.liu@berkeley.edu, Phone: 510-664-7596.
[a]These authors contributed equally to the work presented in this paper.

Introduction

The course of normal human brain development and aging provides a foundation for the understanding of pathological brain degeneration. As such, longitudinal magnetic resonance imaging (MRI) atlases play an important role in understanding the evolution of human brains. The most commonly used atlases for MRI research are mainly based on anatomical features derived from T1- and T2-weighted images. For example, the well-known International Consortium of Brain Mapping (ICBM) atlas (Collins, Holmes et al. 1995, Mazziotta, Toga et al. 2001) and the Talairach atlas (Talairach and Tournoux 1988, Lancaster, Woldorff et al. 2000) both provide target T1-weighted templates for normalization-based group analysis. T2-weighted MRIs are commonly used for fetus and neonate atlas construction (Serag, Aljabar et al. 2012, Shi, Wang et al. 2014, Wei, Zhang et al. 2016).

Quantitative susceptibility mapping (QSM) provides a novel contrast, particularly in iron-rich deep-brain nuclei and white matter fiber bundles (Deistung, Rauscher et al. 2008, de Rochefort, Liu et al. 2010, Liu 2010, Wharton, Schäfer et al. 2010, Liu, Li et al. 2012, Carpenter, Li et al. 2016, Wei, Xie et al. 2016). This is attributed to the sensitivity of QSM to the spatial variations of molecular or cellular components that exhibit different magnetic susceptibility properties. As indicated by several recent studies (Shmueli, de Zwart et al. 2009, Haacke, Miao et al. 2010), magnetic susceptibility of the human brain is mainly influenced by iron and myelin. Human brain myelination and iron deposition evolve over the whole lifespan (Hallgren and Sourander 1958, Lebel, Gee et al. 2012), which is a critical factor in the characterization of early-life brain development and also in the recognition of normative and pathological brain evolution in later-life (Lotfipour, Wharton et al. 2012).

Although there have been susceptibility atlases proposed for certain age groups (Lim, Faria et al. 2013), a longitudinal statistical atlas constructed from the general healthy population based on QSM is still lacking. Registering brains of subjects across the whole lifespan to a common atlas is currently not practical due to large variations in tissue contrast and brain anatomy. For various neurological and psychiatric studies based on iron-rich deep gray matter nuclei, automated co-registration between subject and atlas allows efficient segmentation of the subject brain into regions of interest (ROI) from the atlas. Yet, the existing studies on QSM for aging and neurological disorders are based on group-wise quantitative analysis in a few manually annotated regions of interests (ROIs) (Li, Wu et al. 2014, He, Ling et al. 2015). A robust common QSM template throughout lifespan is greatly needed.

Hence, in the present work, we create a longitudinal QSM atlas using image registration guided by novel fused QSM and T1-weighted images. These two types of contrast are complementary as T1 provides excellent contrast between cortical gray white matter while QSM provides excellent contrast in the iron-rich deep gray matter (Hanspach, Dwyer et al. 2017). By generating group-wise co-registered age-specific brain atlases over various intervals from ages 1 – 83 years, a longitudinal atlas was generated by co-registering age-specific atlases across different age intervals.

Based on the proposed atlas, we created an accurate deep gray matter nuclei parcellation map (DGM map), which includes 9 regions of interest: the dentate nucleus (DN), red nucleus (RN), substantia nigra (SN), caudate nucleus (CN), putamen (PU), globus pallidus (GP), hippocampus (HiP), amygdala (AL) and thalamus (Thal). The thalamus was further segmented into 5 sub-regions, i.e. the anterior nuclei, the median nuclei, the lateral nuclei, the pulvinar and the internal medullary lamina. Finally, we built the "whole brain QSM parcellation map" of 204 ROIs, by combining AAL2 brain parcellation (Rolls, Joliot et al. 2015), JHU DTI-based white-matter atlases (Mori, Wakana et al. 2005), and the proposed DGM map. This proposed whole brain parcellation map allowed automated and accurate segmentation of gray matter and white matter structures for the analysis of QSM data.

1. Methods

An overview of the procedure for the 4D atlas construction and whole-brain ROI-based magnetic susceptibility analysis is presented in Fig. 1.

1.1. Longitudinal atlas construction

1.1.1 Data Acquisition and Reconstruction—A total of 166 healthy subjects (74 M/92 F) with an age range of 1–83 years old were included in the study. The subjects were scanned either at the Brain Imaging and Analysis Center (BIAC) at Duke University, using a 3T scanner (MR 750, GE Healthcare, Milwaukee, WI), or at Rui Jin Hospital (Shanghai, China), using a 3T scanner (Signa HDxt, GE Healthcare, Milwaukee, WI). Imaging was carried out with approval of the institutional review board and informed consent from the adult subjects and parental consent for babies. Conventional T1-weighted images with 1mm isotropic resolution were acquired to display brain structure. Thereafter, a three-dimensional multi-echo gradient echo (GRE) sequence was utilized to obtain T2*-weighted images with the following scan parameters:

The 8 infant subjects (age 1–2 years, 4M/4F) were scanned using a GE MR750 3T with echo time (TE) = 40 ms, repetition time (TR) = 50 ms, and an original spatial resolution of $1 \times 1 \times 1$ mm^3. Infants were scanned without being sedated and were fed before scanning. Neonatal earmuffs were used for hearing protection, and possible motion artifacts were mitigated by immobilization with a cotton pillow. An experienced neonatologist and a neuroradiologist were in attendance throughout the imaging process. A pulse oximeter was used to monitor heart rate and oxygen saturation. The 22 children (age 2–10 years, 8M/14F) subjects were scanned using a GE MR750 3T with TE_1/spacing/TE_8 = 5/2.94/25.6 ms, TR = 55 ms, and an original spatial resolution of $0.6 \times 0.6 \times 1.5$ mm^3. The 19 teenage (age 11–20 years, 10M/9F) subjects were scanned using a GE MR750 3T scanner with TE_1/spacing/TE_8 = 4/2.82/29.4 ms, TR = 41 ms, and an original spatial resolution of $0.86 \times 0.86 \times 2$ mm^3. The 117 adults (age 21–83 years, 52M/65F) subjects were scanned on a GE Signa HDxt 3T scanner with TE_1/spacing/TE_8 = 5.468/3/26.5 ms, TR = 54.6 ms, and an original spatial resolution of $0.86 \times 0.86 \times 2.0$ mm^3.

As the imaging protocols and scanners employed varied among the scans, all the images were resampled to the same spatial resolution of $1 \times 1 \times 1$ mm^3 through operations in k-space in order to minimize the impact of the varying scan parameters.

QSM reconstruction was performed in STI Suite V3.0 (https://people.eecs.berkeley.edu/ ~chunlei.liu/software.html). The sum of squares of GRE magnitude images across echo times ($\sum_{i=1}^{p} mag_i^2$, $i = 1, 2, \ldots, p$, where p is the number of echoes), was used to mask and extract the brain tissue using the brain extraction tool (BET) in FSL (Smith, Jenkinson et al. 2004). The raw phase was unwrapped using a Laplacian-based phase unwrapping (Schofield and Zhu 2003, Li, Wu et al. 2011). The normalized phase ψ was calculated as:

$\psi = \frac{\sum_{i=1}^{n} \omega_i}{\gamma \mu_0 H_0 \sum_{i=1}^{n} TE_i}$ where ω is the unwrapped phase. The normalized background phase was removed with the spherical mean value (SMV) method (Schweser, Deistung et al. 2011, Wu, Li et al. 2012). The variable radius of the SMV filter increased from 1 pixel at the brain boundary to 25 towards the center of the brain with truncated singular value decomposition of 0.05 for the SMV filter during the deconvolution process (Wu, Li et al. 2012). Finally, QSM inversion was applied to the filtered phase using the STAR-QSM algorithm (Wei, Dibb et al. 2015, Wei, Zhang et al. 2016). Susceptibility values were referenced to the mean susceptibility of the whole brain as it has previously been shown that no obvious systematic bias is observed between analysis with and without referencing to CSF (Li, Wu et al. 2014).

1.1.2 Image Pre-processing—The skull was removed from both the GRE magnitude image and the T1-weighted image using FSL BET (Smith, Jenkinson et al. 2004). The T1-weighted (T1w) images were then co-registered to the corresponding magnitude images using FSL FLIRT (Smith, Jenkinson et al. 2004). Thus, the QSM images and T1-weighted image were placed in the same space. The intensity of T1-weighted image was normalized to range [0,255]. Lastly, the QSM(T1w) hybrid images were generated according to the following formula, also as shown in Fig. 1 of (Zhang, Wei et al. 2017):

$$QSM(T1w) = \mu * T1w - QSM \quad (1)$$

where μ is a scalar weighting variable, empirically set to 0.0025 in this study. The combined hybrid images preserve both the enhanced anatomical contrast of deep brain nuclei in the susceptibility map and the clear cortical gray and white matter boundaries defined in the T1-weighted image.

1.1.3 Longitudinal atlas construction—For atlas construction, the subjects were divided by age intervals as shown in Fig 2. Subjects under 10 years-old were separated into 3 age groups: infant group 1–2 years, toddler group 3–4 years and child group 5–10 years; subjects between 11–20 years are divided into 2 groups: the pre-pubertal (11–14 years for girls and 11–15 years for boys) and post-pubertal (15–19 years for girls and 16–19 years for boys) groups (Cameron and Bogin 2012). The remaining 117 adult subjects were divided into 6 age groups in 10-year intervals, (i.e., 21–30 years old, …, 71–80 years old). Fig. 2 shows the number of subjects and gender distribution in each age group for the atlas construction.

A two-step registration strategy was implemented as shown in Fig. 3. Firstly, a group-wise registration algorithm (Wu, Jia et al. 2010, Wu, Jia et al. 2011, Zhang, Shi et al. 2016, Zhang

and Wei 2017) was applied within each age interval to produce an age-specific atlas (Fig. 3 (a) & (b)). A longitudinal registration was then performed across different age intervals to generate the longitudinal common atlas space (Fig. 3 (c)). In the first step, the QSM(T1w) hybrid images of different subjects in the same age group were aligned to form an *Age-specific atlas space*. Specifically, given a set of N hybrid images $\left\{ I_n^{Age^k} \in \mathbb{R}^3 | n=1, \cdots, N \right\}$ within the k-th age group$\{Age^k \in \mathbb{R} | k = 1, \cdots, K\}$, where $K = 11$ denotes the total number of age intervals, the age-specific atlas space was produced using transformations $\left\{ \varphi_n^{Age^k} | n=1, \cdots, N \right\}$, where $\varphi_n^{Age^k}$ denotes the deformation field for the n-th subject within the k-th age group. The average anatomy of a certain age group $Atlas^{Age^k}$ was then calculated by:

$$Atlas^{Age^k} = \frac{1}{N} \sum_{n=1}^{N} I_n^{Age^k} \circ \varphi_n^{Age^k} \qquad (1)$$

where $\circ$ represents the operation of applying the deformation field $\varphi_n^{Age^k}$ to the individual image $I_n^{Age^k}$. In the second step, a longitudinal registration was performed on the age-specific atlases (Fig. 3 (c)). The age-specific atlases $\{Atlas^{Age^1}, \cdots, Atlas^{Age^k}, \cdots, Atlas^{Age^K}\}$ were aligned using the group-wise registration method (Wu, Jia et al. 2010, Wu, Jia et al. 2011). A set of transformations $\left\{ \varphi_{Atlas^{Age^1} \to \overline{Atlas}}, \cdots, \varphi_{Atlas^{Age^k} \to \overline{Atlas}} \right\}$ connects the age-specific templates to produce the *Longitudinal atlas*. Finally, we propagated deformation fields that are produced by the two-step group-wise registration procedure on the individual QSM and T1-weighted images, respectively, to generate the longitudinal QSM and T1-weighted atlases (Fig. 3 (d) & (e)).

1.1.4 Atlas segmentation—For each of the age-specific QSM atlas, we generate a "whole brain QSM parcellation map". Considering the substantial brain anatomical variation through life-time, we strategized different ways to create the parcellation map for different age group. The JHU infant atlas (Oishi, Mori et al. 2011), which provided 122 brain parcellation map and multiple MRI contrast (T1-w, T2-w and DTI), is used for infant QSM atlas segmentation. From age 3–20 years, human brain anatomy undergoes rapid maturation, the segmentation of atlases is processed respectively based on structural MR contrast (T1-w). For adults (>21 years-old), the brain anatomy is relatively stable, susceptibility development turns into the most essential variation with aging. For atlas from age 21 to age 80, the parcellation maps are created based on the longitudinal QSM atlas (as presented in Fig. 4), in order to keep the parcellation map consistent between each specific age interval. The detailed procedure for QSM atlas segmentation is presented below respectively.

1. For infant atlas (age 1–2 years), the JHU infant atlas (Oishi, Mori et al. 2011) was registered towards the proposed T1-weighted infant atlas via FSL affine registration (FLIRT) (Smith, Jenkinson et al. 2004) followed by diffeomorphic registration (DEMONS) (Vercauteren, Pennec et al. 2009). The deformation

fields were then applied to the JHU infant 122 parcellation map (Oishi, Mori et al. 2011) for propagating the parcellation to the infant QSM atlas.

2. For atlases from age 3 to 20 years, the ICBM 152 T1-weighted atlas (Fonov, Evans et al. 2009) was registered towards each of the age-specific T1-weighted atlas via FSL affine registration (FLIRT) (Smith, Jenkinson et al. 2004) followed by diffeomorphic registration (DEMONS) (Vercauteren, Pennec et al. 2009). The deformation fields were then applied to the AAL2 (Rolls, Joliot et al. 2015) parcellation map and the JHU DTI-based white-matter atlases (Mori, Wakana et al. 2005, Wakana, Caprihan et al. 2007, Hua, Zhang et al. 2008) to warp the cortical and white matter fiber bundle ROIs into the age-specific QSM atlas space from age 3 to 20 years.

3. For atlas from age 21 to age 80, the parcellation maps are created based on the longitudinal QSM atlas. As shown in Fig. 4, the ICBM 152 T1-weighted atlas (Fonov, Evans et al. 2009) was registered towards the proposed longitudinal T1-weighted atlas via FSL affine registration (FLIRT) (Smith, Jenkinson et al. 2004) followed by diffeomorphic registration (DEMONS) (Vercauteren, Pennec et al. 2009). The deformation fields were then applied to the AAL2 (Rolls, Joliot et al. 2015) parcellation map and the JHU DTI-based white-matter atlases (Mori, Wakana et al. 2005, Wakana, Caprihan et al. 2007, Hua, Zhang et al. 2008) to warp the cortical and white matter fiber bundle ROIs into the longitudinal QSM atlas space (Fig. 4 step 2).

Considering the relatively weak contrast of brain nuclei on T1-weighted images, from the existing parcellation maps for each age group referenced above, we removed 12 ROIs, including the bilateral caudate nucleus (CN), putamen (PU), globus pallidus (GP), hippocampus (HiP), amygdala (AL) and thalamus (Thal), and manually created these ROIs using the proposed QSM atlas (Fig. 4 (a)). Benefitting from the distinct contrast between iron-rich nuclei and white matter bundles in QSM images, we were able to observe the sub-structure of thalamus. We therefore propose a novel thalamus parcellation map. Thalamic nuclei have previously been delineated on an ex vivo basis, exploiting the differing chemoarchitectual and cytoarchitectual properties of the various cellular populations to identify unique, functionally specialized territories (Schmahmann 2003, Jacobson and Marcus 2011, Renard, Castelnovo et al. 2014). With reference to the anatomical structure of thalamus in previous studies, 10 sub-regions were labeled in the bilateral thalamus: the anterior nuclei, the median nuclei, the lateral nuclei, the pulvinar nuclei and the internal medullary lamina. Thus, in total, we added 22 deep gray matter nuclei ROIs. Finally, AAL2, DTI-based white matter and the proposed deep gray matter maps were combined to create the "whole brain QSM parcellation map" as shown in Fig. 4, step 3.

The built atlases will be included in the STI Suite software package and can be downloaded from https://people.eecs.berkeley.edu/~chunlei.liu/software.html.

1.1.5 ROI-based Image Analysis

1.1.5.1 Atlas based QSM image segmentation: Using the newly built QSM parcellation map, an accurate segmentation of deep-brain nuclei in individual images was achieved.

For subjects with age 1–20 years, individual QSM images with various ages were registered to the closest age-specific atlas thus obtaining the most accurate ROI segmentation. This algorithm can be expressed as:

$$S_n^{Age^k} = Seg^{Age^k} \circ (\varphi_n^{Age^k})^{-1} \quad (3)$$

where $S_n^{Age^k}$ denotes the ROI segmentation for each individual QSM image, Seg^{Age^k} denotes the parcellation map for each age-specific QSM atlas,

For adults, as shown in Fig. 5, the parcellation map in the proposed longitudinal atlas space was first backtracked to each age-specific atlas space, using the inverted transformations fields $\left\{ (\varphi_{Atlas^{Age1} \to \overline{Atlas}})^{-1}, \cdots, (\varphi_{Atlas^{Age^k} \to \overline{Atlas}})^{-1} \right\}$, and was further warped to fit with each individual QSM image. Benefitting from the longitudinal age-specific atlases, individual QSM images from subjects with various ages were registered to the closest age-specific atlas thus obtaining the most accurate ROI segmentation. This algorithm can be expressed as:

$$S_n^{Age^k} = Seg^{Age^k} \circ (\varphi_n^{Age^k})^{-1} = \overline{Seg} \circ (\varphi_{Atlas^{Age^k} \to \overline{Atlas}})^{-1} \circ (\varphi_n^{Age^k})^{-1} \quad (4)$$

where $\overline{Seg}$ is the parcellation map in the longitudinal atlas space.

1.1.5.2 Segmentation accuracy evaluation: In order to assess the atlas-based QSM image segmentation accuracy, we built 3 test datasets. These datasets are independent of the subjects used for atlas construction. **Test dataset 1** contains ten child subjects, comprising three subjects aged 1–2 years-old, three subjects aged 3 years old, one subject aged 6 years-old, two subjects aged 7 years-old, and one subject aged 11 years-old. **Test dataset 2** contains junior adult subjects, comprised of 15 subjects aged 25–46 years-old. **Test dataset 3** contains senior adult subjects, comprised of 15 subjects aged 63–80 years-old. The manual segmentations of 6 deep gray matter nuclei (CN, PU, GP, RN, SN and DN) were carried out by three experienced radiologists. For assessing intra-rater reliability, we asked the raters drew the ROIs on each subject two times, with one week in between sessions. To eliminate individual annotation bias, the majority voting of the six ROI annotations (three raters, two times) is defined as the ground truth. We compare the ground truth and the automated ROI labelling of the bilateral deep gray matter nucleus by means of Dice Ratio: $DR = 2|A \cap B|/(|A| + |B|)$. DR ranges from 0 (for totally disjoint segmentations) to 1 (for identical segmentations). The structural agreement was calculated in each pair of automatically labelled and ground truth ROIs.

1.2. Fitting susceptibility development in the deep gray matter nuclei

As presented in the previous section, individual QSM images are segmented using the proposed QSM atlases. We can thus calculate the mean susceptibility value of each ROI for further analysis. In this section, we investigated the specific progression of the iron

deposition in deep gray matter nuclei, hippocampus, amygdala and thalamic nuclei over the lifespan using susceptibility maps.

Progressive accumulation of iron with aging has been well reported in brain tissues (Hallgren and Sourander 1958). As iron content is the main contributor to the bulk magnetic susceptibility in deep gray nuclei (Schweser, Deistung et al. 2011), the susceptibility development can be modeled using the exponential growth model (Li, Wu et al. 2014), which was originally proposed by Hallgren et al. (Hallgren and Sourander 1958) to model the iron concentration development:

$$\chi[ppm] = \alpha \left(1 - exp(-\beta * age[year])\right) + \gamma \quad (5)$$

where χ represents the magnetic susceptibility scalar variables α, β and γ are tissue specific parameters, with β defining the rate of the exponential growth.

2. Results

2.1. Atlas construction

2.1.1 Significance of the hybrid contrast guided atlas construction strategy—
As presented in Sec. 1.1.2, we incorporated QSM and T1-weighted images of each individual to generate the hybrid QSM(T1w) contrast to optimize co-registration in the group-wise atlas construction process. We then propagated the deformation fields that were produced by the two-step group-wise registration procedure to the individual QSM and T1-weighted images respectively, and thus obtained the longitudinal QSM and T1-weighted atlases as shown in Fig. 6 (a). For comparison purposes, we also built group-wise atlases only using T1-weighted images and QSM images, respectively. As shown in Fig. 6 (b) & (c), detailed structure is clearly observed in the proposed atlas with registration guided by hybrid QSM(T1w) images, especially in the cortical regions and deep gray matter regions as indicated by close-views.

Fig. 7 shows twelve representative axial slices of the longitudinal QSM brain atlas constructed by the proposed method, which represents adult brain from age 21 to 83 years. Despite the large number of subjects (117) used for atlas construction, the atlas still preserves structural details both in the cortical regions and deep gray matter regions.

2.1.2 Region of interest creation—
Fig. 8 (a) & (b) show the axial and coronal views of the anatomical structure of the thalamus (Jacobson and Marcus 2011). Fig. 8 (c) & (d) show the axial and coronal views of the proposed QSM atlas thalamus parcellation map showing contrast consistent with Fig. 8 (a) and (b). Fig. 8 (e) & (f) indicate the 3D rendering of the thalamus parcellation map, which is set in the background of the maximum intensity projection of the longitudinal QSM atlas.

Fig. 9 (a) shows the cortical parcellation map propagated from the AAL2 atlas (Rolls, Joliot et al. 2015), which was derived from T1-weighted contrast. The 12 ROIs for deep gray matter nuclei were removed from AAL2 and manually drawn on the proposed longitudinal

QSM atlas, as shown in Fig. 9 (c). Since the thalamus was segmented into 10 sub-regions, the number of deep gray matter ROIs was extended to 22. Fig. 9 (b) shows representative slices containing white-matter ROIs, which was created from JHU DTI-based white-matter atlas (Mori, Wakana et al. 2005, Wakana, Caprihan et al. 2007, Hua, Zhang et al. 2008). Fig. 9 (d) shows the whole brain QSM parcellation map, formed by combining the ROIs delineated by the warped AAL2, the JHU DTI white-matter atlas and the proposed DGM map in the axial, sagittal, and coronal planes, respectively. The infant QSM atlas parcellation map is shown in Fig. 7 in reference (Zhang, Wei et al. 2017).

2.1.3 Automated ROI annotation for assessing accuracy of segmentation—For assessing intra-rater and inter-rater ROI segmentation reliability, the overall average Dice Ratios (DRs) of each ROIs for each test dataset was presented in Table 1. The mean intra & inter-rater DRs for the child (dataset1), junior adult (dataset2), senior adult (dataset3) test dataset are higher than 0.81, 0.84, 0.84, respectively, which shows excellent agreement between each rater and each segmentation (each rater labeled twice). The segmentation ground truth for each ROI is defined by the majority voting from the three raters. Then each rater's segmentation and the automated segmentation (using the proposed age-specific QSM atlas) are compared with the ground truth as shown in Table 1. For all the three datasets, the automated segmentation shows comparable accuracy to the raters' segmentation.

For further comparison, the ICBM 152 T1-weighted atlas (Fonov, Evans et al. 2009), the Pediatric atlas (Fonov, Evans et al. 2011), the JHU EveQSM (Lim, Faria et al. 2013) atlas, the proposed longitudinal and age-specific atlases were included in the accuracy assessment. For each atlas and each test data image, the individual image was first aligned to the atlas and the inverted deformation field was applied to the atlas parcellation map, generating the individual parcellation map. For each subject, we chose the atlas with the most similar age, e.g., for a subject at 7 years of age, we use the T1 pediatric atlas for 7.0–11.0 years-old and our proposed QSM age-specific atlas for 6–10 years-old.

Statistical analysis results are shown in Fig. 10 (a). It is shown that the proposed atlases outperform the T1-weighted atlases and the JHU EveQSM atlas, for all the three test datasets. For the children dataset (dataset1), the dice ratio of the proposed longitudinal QSM atlas is slightly higher than that of the EveQSM atlas, while the age-specific QSM atlas makes further improvement. As shown in section 2.2, the susceptibility in the iron-rich nuclei varied dramatically with aging. Thus the pediatric QSM atlases provided the most appropriate reference for children brain nuclei annotation. For both junior and senior adult test datasets (datasets 2 & 3), the accuracy of the proposed longitudinal and age-specific QSM atlas is higher than the EveQSM atlas.

The estimates of tissue volume for the three datasets are shown in Fig. 10 (b). Notably, for the child test dataset, the proposed age-specific atlas shows significant improvement for estimating Dentate Nucleus (DN) volume. The DN in the infant brain shows inverted contrast compared to that of adult brain in QSM. Thus, it is crucial to use a specific atlas for child brain analysis. Fig. 10 (c) shows the estimation of mean susceptibility in each dataset. Compared with the ground truth, segmentation based on the T1-weighted atlases produces lower susceptibility values, while the QSM-atlas based segmentation yields higher

susceptibility values. As shown in Fig. 10 (b), the ICBM T1-based atlas annotated larger regions for iron-rich brain nuclei, thus yielding lower susceptibility values due to the erroneous inclusion of surrounding tissues. In contrast, the QSM-based atlases provided relatively robust segmentations, resulting in a higher susceptibility values. Considering the Dice Ratio, tissue volume and susceptibility estimations, the proposed age-specific atlases provide the most accurate deep gray matter nuclei segmentation, and shows outstanding improvement especially for child QSM image segmentation.

2.2. Susceptibility development with age

Using the proposed age-specific QSM atlases, we conducted atlas-based automated individual QSM image segmentation, then measured the susceptibility development of caudate nucleus (CN), putamen (PU), globus pallidus (GP), red nucleus (RN), substantia nigra (SN), dentate nucleus (DN), hippocampus (HiP), amygdala (AL) and thalamic (Thal) nuclei with normal aging.

Deep gray matter nucleus development—Close-up views of the putamen (PU), globus pallidus (GP), and caudate nucleus (CN) in each age-specific atlas are presented in Fig. 2 in reference (Zhang, Wei et al. 2017). The susceptibility contrast between the 3 deep gray matter ROIs and their surroundings is relatively low in the infant (<2 years) and children (3–5 years & 7–10 years) brains, which indicates less iron content stored in the 3 nuclei (Deistung, Schäfer et al. 2013) and less myelination in the surrounding white matter fibers (Pujol, López-Sala et al. 2004, Deoni, Dean et al. 2012). For infants, children and teenagers (11–20 years), the inner and outer GP can be distinguished well based on magnetic susceptibility differences. Anatomically, the inner and outer GP is physically separated by medial medullary lamina, which becomes thinner with human brain maturation (>21 years-old) resulting a blurred delineation between the two. For the adult atlases, susceptibility inhomogeneity within PU becomes apparent as age increases, and the susceptibility becomes more paramagnetic with age. This is consistent with previous findings that iron accumulation follows a precise direction from posterior to the anterior in PU (Aquino, Bizzi et al. 2009).

Fig. 3 in reference (Zhang, Wei et al. 2017) shows the enlarged RN and SN regions in the age-specific QSM atlases. The susceptibility contrast between the deep gray matter and its surroundings is relatively low in infant and child brains. The mean susceptibility within each region shows increasing contrast between the SN and RN and the surrounding brain tissues. For infants, children and teenagers, we can observe part of the globus pallidus (GP) above the SN. For the older atlases (over 21 years), only a very small part of GP can be observed. This observation indicates that the positions of RN and SN in the minors are relatively closer to the GP than those observed in adult brains. This is consistent with previous findings that the morphology of sub-thalamic nucleus, changes locally with age (Keuken, Bazin et al. 2013).

Fig. 4 in reference (Zhang, Wei et al. 2017) shows the enlarged DN regions in the age-specific QSM atlases. The susceptibility contrast between the DN and its surroundings varies

significantly with age. In infants, the susceptibility is lower in the DN than in surrounding tissues. The DN become brighter with aging due to the increasing iron deposition.

As shown in the top two rows of Fig. 6 in reference (Zhang, Wei et al. 2017), we collected the average susceptibility value in six iron-rich deep gray matter ROIs (CN, PU, GP, RN, SN and DN) from each individual subject (age 1–83 years), then fitted the collected aging data to the exponential model in Eq. (5). The regression fitting models of the mean susceptibility in each ROI are listed in Table 2.

Hippocampus and amygdala development—As shown in the bottom row of Fig. 6 in reference (Zhang, Wei et al. 2017), the development of susceptibility values in hippocampus and amygdala can be characterized by fitting to the exponential growth model (Eq. (5)). This finding suggests that susceptibility development of hippocampus and amygdala is likely dominated by iron deposition.

Thalamic nuclei development—Zoomed-in views of the thalamus in each age-specific atlas are presented in Fig. 11. The magnetic susceptibility of thalamic nuclei varies diversely in different sub-regions. The susceptibility of thalamus anterior nuclei and pulvinar become more paramagnetic with aging. In the infant and children brain, the anterior nuclei display lower susceptibility compared to the surrounding brain tissues; in 21–30 years and 31–40 years atlases, the contrast between anterior nuclei and their surroundings is relatively low; in the later age (>41 years) atlases, the anterior nuclei become brighter. In the median and lateral nuclei, the susceptibility initially increases, then decreases with aging (Fig. 12). While the susceptibility of the internal medullary lamina shows a monotonous decrease with aging.

The iron deposition with aging in thalamus has been reported to follow an unusual development (Hallgren and Sourander 1958). Distinct from other brain regions, iron content in thalamus appears a rise-up to about 35 years-old, then turns to a decline till 90 years-old (Fig. 12 (a) (Hallgren and Sourander 1958)). We investigate the susceptibility changes in the whole thalamus region, the thalamic nuclei, the anterior nuclei, the pulvinar, the lateral nuclei, the medial nuclei and the internal medullary lamina respectively. As indicated in Fig. 12 (b), in the whole thalamus region, the susceptibility development indicates an initial increase from 1–35 years-old and followed by a decrease in the later age. In order to investigate more accurate iron-related susceptibility development, we excluded the internal medullary lamina which mainly contains white matter fiber tracts. The susceptibility change in thalamic nuclei (Fig 12 (c)) shows sharper increase and decrease than that in the whole thalamus (Fig 12 (b)). This development trend is consistent with the iron deposition trend reported by Hallgren et al. (Hallgren and Sourander 1958), which indicates the susceptibility development in the thalamus region is substantially determined by iron content. As shown in Fig. 12 (d) & (e), the susceptibility developments in the anterior nuclei and pulvinar follow the exponential growth model (Eq. (5)), which suggests iron accumulation with aging in the two nuclei. Especially, the susceptibility value evolves asymmetrically in the bi-lateral anterior nuclei. After 20 years of age, the susceptibility in the left anterior nucleus is higher than in the right one for both male and female (Fig. 12 (d)). For the lateral nuclei and the medial nuclei, our result shows the bidirectional patterns with an initial increase followed by

a decrease in susceptibility (Fig. 12 (f) & (g)). This suggests that the decline of iron content in thalamus, starting around age of thirty/forty, proceeds essentially in the medial and lateral nuclei. While in the internal medullary lamina, we observe a monotonic decrease in susceptibility which is mainly diamagnetic as shown in Fig. 12 (h). In different sub-regions of thalamus, the susceptibility developments show a variety of patterns, which indicates distinct characteristics of brain tissue component development in thalamic nuclei.

3. Discussion and limitations

In the present study, the subject number across age is not evenly distributed. The number of senior adult (>41 years-old) is much higher than that of junior adult, adolescent, children and infant. The strategy of building age-specific atlas overcomes the bias related to age on building the longitudinal atlas, but the lack of young participants restricted us on further specializing age groups such as early childhood (e.g. 5–7) and later childhood (e.g. 8–10). This also caused a few gaps on the susceptibility development curves (e.g. Fig. 12), and might lead to potential bias on the susceptibility developmental trajectory fitting.

The susceptibility development with age in the iron-rich brain nuclei, the hippocampus and the amygdala is modelled using the exponential growth model (Hallgren and Sourander 1958). The fitted trajectories provided systematic confirmation of previous findings on susceptibility progression resulting from manual ROI drawings in deep gray matter nuclei (Li, Wu et al. 2014). However, the bidirectional patterns with an initial increase followed by a decrease in susceptibility (e.g. Fig. 12 (f) & (g)) in the whole thalamus, the thalamic lateral nuclei and the thalamic medial nuclei cannot be fitted using the simple exponential growth model. Although the developmental pattern is supported by Non-haemin iron deposition (Mg Iron/100g fresh tissue weight) development with aging in the thalamus reported by Hallgren and Sourander (Hallgren and Sourander 1958), the undergoing mechanism of the iron loss in the specific nuclei need to be further investigated. More complex and specific sub-regions within the thalamic nuclei can be observed from QSM images at higher spatial resolution using higher field strength (7T) (Deistung, Schäfer et al. 2013). More detailed parcellation map of thalamus via the combination of high-resolution QSM and DTI information is a promising future perspective.

QSM atlas brought significant efficiency for projecting individual QSM into a common space. During the maturation stage, human brain undergoes substantial variations on both anatomy (Cameron and Bogin 2012) and susceptibility (Hallgren and Sourander 1958, Li, Wu et al. 2014). Benefitting from the age-specific QSM atlas under 20 years-old, the annotation accuracy of deep gray matter is significantly improved for infant, children and adolescence subjects. By constructing the longitudinal QSM atlas for matured age group (>21 years), the brain parcellation map consistency with aging is preserved. The proposed age-specific QSM atlases will be available in the STISuite V3.0 software package and can be downloaded at (https://people.eecs.berkeley.edu/~chunlei.liu/software.html). The optimal parcellation performance could be obtained using the closest age-specific atlas. For adult subject lacking age information, the longitudinal QSM atlas also provides precise segmentation.

4. Conclusions

The present work used longitudinal QSM data over the lifespan to construct serial QSM atlases over various age intervals from ages 1 – 83 years based on group-wise registration. The common susceptibility atlases provided a standard coordinate system to conduct group analyses for QSM studies over a large age range. These atlases also provided an efficient tool for segmenting brain structures at specific ages, benefiting from the dramatic delineation between different brain tissues. The regional findings were consistent with known patterns of iron load in deep-brain structures and their variation with aging. The susceptibility atlases also indicated common tissue structure variations at each age interval, which is a critical reference for investigating the brain gray and white matter development with aging. A novel segmentation of the thalamus is provided. The longitudinal QSM atlas is confirmed to be a useful new noninvasive tool for investigating cerebral iron accumulation.

References

Aquino D, Bizzi A, Grisoli M, Garavaglia B, Bruzzone MG, Nardocci N, Savoiardo M, Chiapparini L. Age-related Iron Deposition in the Basal Ganglia: Quantitative Analysis in Healthy Subjects 1. Radiology. 2009; 252(1):165–172. [PubMed: 19561255]

Cameron, N., Bogin, B. Human growth and development. Academic Press; 2012.

Carpenter KL, Li W, Wei H, Wu B, Xiao X, Liu C, Worley G, Egger HL. Magnetic susceptibility of brain iron is associated with childhood spatial IQ. NeuroImage. 2016; 132:167–174. [PubMed: 26899787]

Collins DL, Holmes CJ, Peters TM, Evans AC. Automatic 3-D model-based neuroanatomical segmentation. Human brain mapping. 1995; 3(3):190–208.

de Rochefort L, Liu T, Kressler B, Liu J, Spincemaille P, Lebon V, Wu J, Wang Y. Quantitative susceptibility map reconstruction from MR phase data using bayesian regularization: validation and application to brain imaging. Magnetic Resonance in Medicine. 2010; 63(1):194–206. [PubMed: 19953507]

Deistung A, Rauscher A, Sedlacik J, Stadler J, Witoszynskyj S, Reichenbach JR. Susceptibility weighted imaging at ultra high magnetic field strengths: theoretical considerations and experimental results. Magnetic Resonance in Medicine. 2008; 60(5):1155–1168. [PubMed: 18956467]

Deistung A, Schäfer A, Schweser F, Biedermann U, Turner R, Reichenbach JR. Toward in vivo histology: a comparison of quantitative susceptibility mapping (QSM) with magnitude-, phase-, and R 2*-imaging at ultra-high magnetic field strength. Neuroimage. 2013; 65:299–314. [PubMed: 23036448]

Deoni SC, Dean DC, O'muircheartaigh J, Dirks H, Jerskey BA. Investigating white matter development in infancy and early childhood using myelin water faction and relaxation time mapping. Neuroimage. 2012; 63(3):1038–1053. [PubMed: 22884937]

Fonov V, Evans AC, Botteron K, Almli CR, McKinstry RC, Collins DL, Group BDC. Unbiased average age-appropriate atlases for pediatric studies. Neuroimage. 2011; 54(1):313–327. [PubMed: 20656036]

Fonov VS, Evans AC, McKinstry RC, Almli C, Collins D. Unbiased nonlinear average age-appropriate brain templates from birth to adulthood. NeuroImage. 2009; 47:S102.

Haacke EM, Miao Y, Liu M, Habib CA, Katkuri Y, Liu T, Yang Z, Lang Z, Hu J, Wu J. Correlation of putative iron content as represented by changes in R2* and phase with age in deep gray matter of healthy adults. Journal of Magnetic Resonance Imaging. 2010; 32(3):561–576. [PubMed: 20815053]

Hallgren B, Sourander P. The effect of age on the non-haemin iron in the human brain. Journal of neurochemistry. 1958; 3(1):41–51. [PubMed: 13611557]

Hanspach J, Dwyer MG, Bergsland NP, Feng X, Hagemeier J, Bertolino N, Polak P, Reichenbach JR, Zivadinov R, Schweser F. Methods for the computation of templates from quantitative magnetic

susceptibility maps (QSM): Toward improved atlas-and voxel-based analyses (VBA). Journal of Magnetic Resonance Imaging. 2017

He N, Ling H, Ding B, Huang J, Zhang Y, Zhang Z, Liu C, Chen K, Yan F. Region-specific disturbed iron distribution in early idiopathic Parkinson's disease measured by quantitative susceptibility mapping. Human brain mapping. 2015; 36(11):4407–4420. [PubMed: 26249218]

Hua K, Zhang J, Wakana S, Jiang H, Li X, Reich DS, Calabresi PA, Pekar JJ, van Zijl PC, Mori S. Tract probability maps in stereotaxic spaces: analyses of white matter anatomy and tract-specific quantification. Neuroimage. 2008; 39(1):336–347. [PubMed: 17931890]

Jacobson, S., Marcus, EM. Neuroanatomy for the Neuroscientist. Springer Science & Business Media; 2011.

Keuken MC, Bazin PL, Schäfer A, Neumann J, Turner R, Forstmann BU. Ultra-high 7T MRI of structural age-related changes of the subthalamic nucleus. Journal of Neuroscience. 2013; 33(11): 4896–4900. [PubMed: 23486960]

Lancaster JL, Woldorff MG, Parsons LM, Liotti M, Freitas CS, Rainey L, Kochunov PV, Nickerson D, Mikiten SA, Fox PT. Automated Talairach atlas labels for functional brain mapping. Human brain mapping. 2000; 10(3):120–131. [PubMed: 10912591]

Lebel C, Gee M, Camicioli R, Wieler M, Martin W, Beaulieu C. Diffusion tensor imaging of white matter tract evolution over the lifespan. Neuroimage. 2012; 60(1):340–352. [PubMed: 22178809]

Li W, Wu B, Batrachenko A, Bancroft-Wu V, Morey RA, Shashi V, Langkammer C, Bellis MD, Ropele S, Song AW. Differential developmental trajectories of magnetic susceptibility in human brain gray and white matter over the lifespan. Human brain mapping. 2014; 35(6):2698–2713. [PubMed: 24038837]

Li W, Wu B, Liu C. Quantitative susceptibility mapping of human brain reflects spatial variation in tissue composition. Neuroimage. 2011; 55(4):1645–1656. [PubMed: 21224002]

Lim IAL, Faria AV, Li X, Hsu JT, Airan RD, Mori S, van Zijl PC. Human brain atlas for automated region of interest selection in quantitative susceptibility mapping: application to determine iron content in deep gray matter structures. Neuroimage. 2013; 82:449–469. [PubMed: 23769915]

Liu C. Susceptibility tensor imaging. Magnetic resonance in medicine. 2010; 63(6):1471–1477. [PubMed: 20512849]

Liu C, Li W, Wu B, Jiang Y, Johnson GA. 3D fiber tractography with susceptibility tensor imaging. Neuroimage. 2012; 59(2):1290–1298. [PubMed: 21867759]

Lotfipour AK, Wharton S, Schwarz ST, Gontu V, Schäfer A, Peters AM, Bowtell RW, Auer DP, Gowland PA, Bajaj NP. High resolution magnetic susceptibility mapping of the substantia nigra in Parkinson's disease. Journal of Magnetic Resonance Imaging. 2012; 35(1):48–55. [PubMed: 21987471]

Mazziotta J, Toga A, Evans A, Fox P, Lancaster J, Zilles K, Woods R, Paus T, Simpson G, Pike B. A probabilistic atlas and reference system for the human brain: International Consortium for Brain Mapping (ICBM). Philosophical Transactions of the Royal Society of London B: Biological Sciences. 2001; 356(1412):1293–1322. [PubMed: 11545704]

Mori, S., Wakana, S., Van Zijl, PC., Nagae-Poetscher, L. MRI atlas of human white matter. Elsevier; 2005.

Oishi K, Mori S, Donohue PK, Ernst T, Anderson L, Buchthal S, Faria A, Jiang H, Li X, Miller MI. Multi-contrast human neonatal brain atlas: application to normal neonate development analysis. Neuroimage. 2011; 56(1):8–20. [PubMed: 21276861]

Pujol J, López-Sala A, Sebastián-Gallés N, Deus J, Cardoner N, Soriano-Mas C, Moreno A, Sans A. Delayed myelination in children with developmental delay detected by volumetric MRI. Neuroimage. 2004; 22(2):897–903. [PubMed: 15193620]

Renard D, Castelnovo G, Campello C, Bouly S, Le Floch A, Thouvenot E, Waconge A, Taieb G. Thalamic lesions: a radiological review. Behavioural neurology. 2014; 2014

Rolls ET, Joliot M, Tzourio-Mazoyer N. Implementation of a new parcellation of the orbitofrontal cortex in the automated anatomical labeling atlas. Neuroimage. 2015; 122:1–5. [PubMed: 26241684]

Schmahmann JD. Vascular syndromes of the thalamus. Stroke. 2003; 34(9):2264–2278. [PubMed: 12933968]

Schofield MA, Zhu Y. Fast phase unwrapping algorithm for interferometric applications. Optics letters. 2003; 28(14):1194–1196. [PubMed: 12885018]

Schweser F, Deistung A, Lehr BW, Reichenbach JR. Quantitative imaging of intrinsic magnetic tissue properties using MRI signal phase: an approach to in vivo brain iron metabolism? Neuroimage. 2011; 54(4):2789–2807. [PubMed: 21040794]

Serag A, Aljabar P, Ball G, Counsell SJ, Boardman JP, Rutherford MA, Edwards AD, Hajnal JV, Rueckert D. Construction of a consistent high-definition spatio-temporal atlas of the developing brain using adaptive kernel regression. NeuroImage. 2012; 59(3):2255–2265. [PubMed: 21985910]

Shi F, Wang L, Wu G, Li G, Gilmore JH, Lin W, Shen D. Neonatal atlas construction using sparse representation. Human brain mapping. 2014; 35(9):4663–4677. [PubMed: 24638883]

Shmueli K, de Zwart JA, van Gelderen P, Li TQ, Dodd SJ, Duyn JH. Magnetic susceptibility mapping of brain tissue in vivo using MRI phase data. Magnetic resonance in medicine. 2009; 62(6):1510–1522. [PubMed: 19859937]

Smith SM, Jenkinson M, Woolrich MW, Beckmann CF, Behrens TE, Johansen-Berg H, Bannister PR, De Luca M, Drobnjak I, Flitney DE. Advances in functional and structural MR image analysis and implementation as FSL. Neuroimage. 2004; 23:S208–S219. [PubMed: 15501092]

Talairach J, Tournoux P. Co-planar stereotaxic atlas of the human brain. 3-Dimensional proportional system: an approach to cerebral imaging. 1988

Vercauteren T, Pennec X, Perchant A, Ayache N. Diffeomorphic demons: Efficient non-parametric image registration. NeuroImage. 2009; 45(1):S61–S72. [PubMed: 19041946]

Wakana S, Caprihan A, Panzenboeck MM, Fallon JH, Perry M, Gollub RL, Hua K, Zhang J, Jiang H, Dubey P. Reproducibility of quantitative tractography methods applied to cerebral white matter. Neuroimage. 2007; 36(3):630–644. [PubMed: 17481925]

Wei H, Dibb R, Zhou Y, Sun Y, Xu J, Wang N, Liu C. Streaking artifact reduction for quantitative susceptibility mapping of sources with large dynamic range. NMR in Biomedicine. 2015; 28(10): 1294–1303. [PubMed: 26313885]

Wei H, Xie L, Dibb R, Li W, Decker K, Zhang Y, Johnson GA, Liu C. Imaging whole-brain cytoarchitecture of mouse with MRI-based quantitative susceptibility mapping. NeuroImage. 2016; 137:107–115. [PubMed: 27181764]

Wei H, Zhang Y, Gibbs E, Chen NK, Wang N, Liu C. Joint 2D and 3D phase processing for quantitative susceptibility mapping: application to 2D echo-planar imaging. NMR in Biomedicine. 2016

Wharton S, Schäfer A, Bowtell R. Susceptibility mapping in the human brain using threshold-based k-space division. Magnetic resonance in medicine. 2010; 63(5):1292–1304. [PubMed: 20432300]

Wu B, Li W, Guidon A, Liu C. Whole brain susceptibility mapping using compressed sensing. Magnetic resonance in medicine. 2012; 67(1):137–147. [PubMed: 21671269]

Wu G, Jia H, Wang Q, Shen D. Groupwise registration with sharp mean. Medical Image Computing and Computer-Assisted Intervention–MICCAI. 2010; 2010:570–577.

Wu G, Jia H, Wang Q, Shen D. SharpMean: groupwise registration guided by sharp mean image and tree-based registration. NeuroImage. 2011; 56(4):1968–1981. [PubMed: 21440646]

Zhang Y, Shi F, Wu G, Wang L, Yap PT, Shen D. Consistent spatial-temporal longitudinal atlas construction for developing infant brains. IEEE transactions on medical imaging. 2016; 35(12): 2568–2577. [PubMed: 27392345]

Zhang Y, Wei H. Atlas construction of cardiac fiber architecture using a multimodal registration approach. Neurocomputing. 2017

Zhang Y, Wei H, He N, Yan F, Liu C. Longitudinal Analysis Data of Magnetic Susceptibility for Normative Human Brain Development and Aging over the Lifespan. 2017 Data in Brief in press.
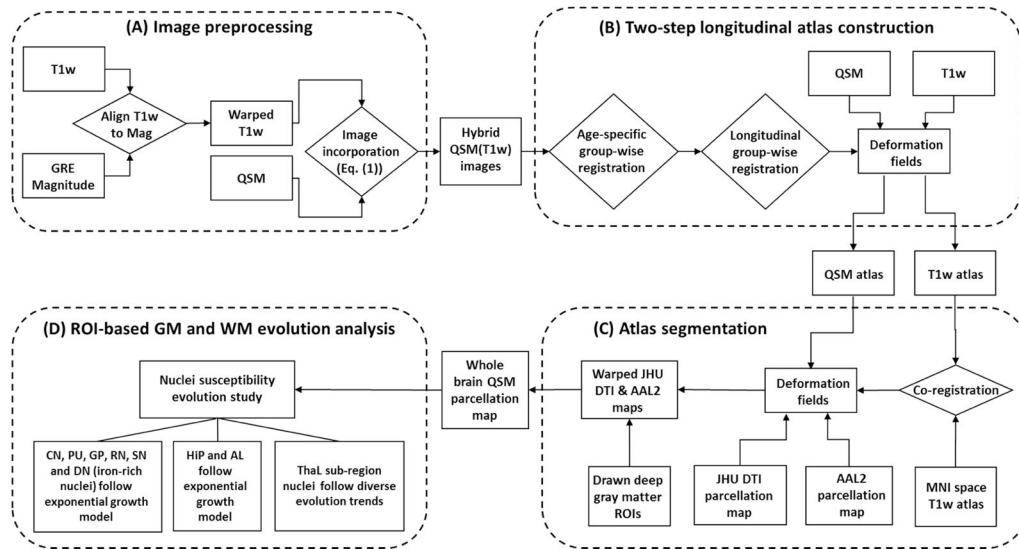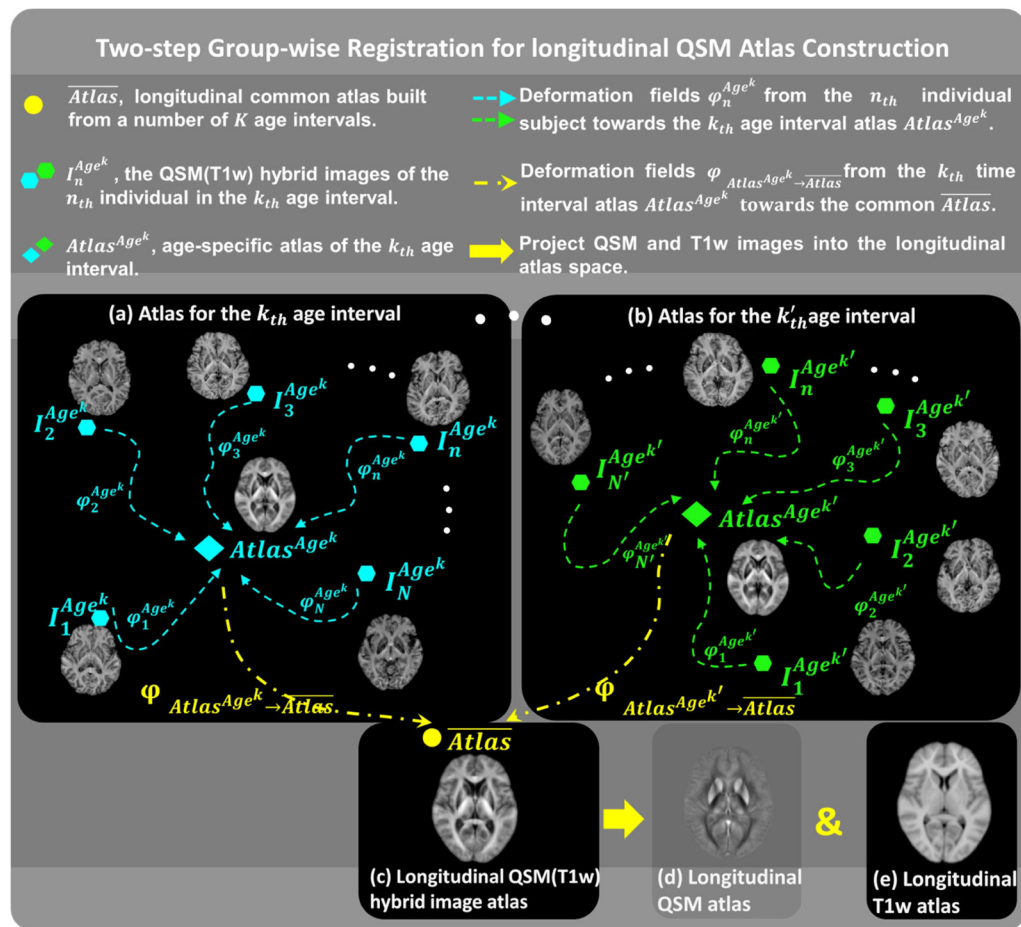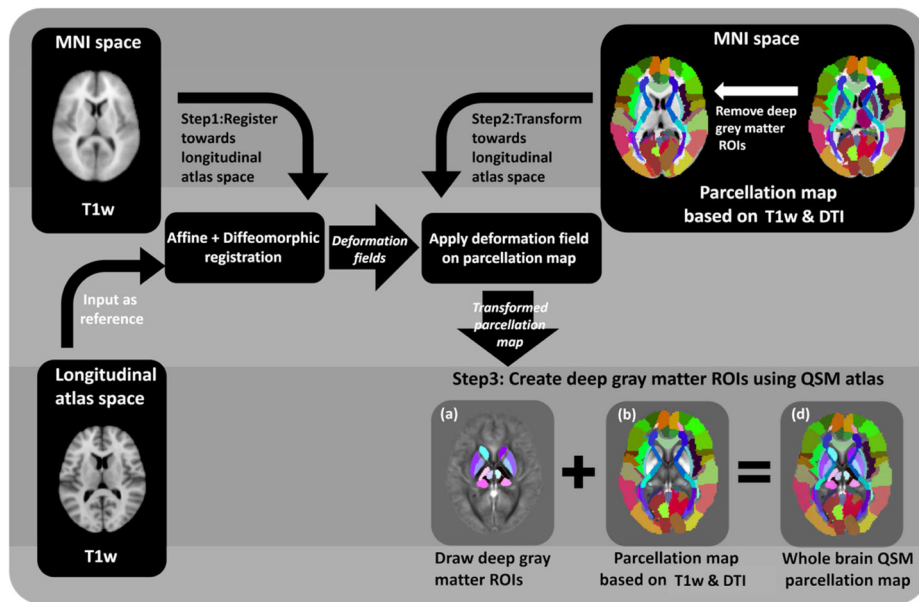
Figure 1.
Flow chart of 4D QSM atlas construction and brain nucleus magnetic susceptibility analysis.
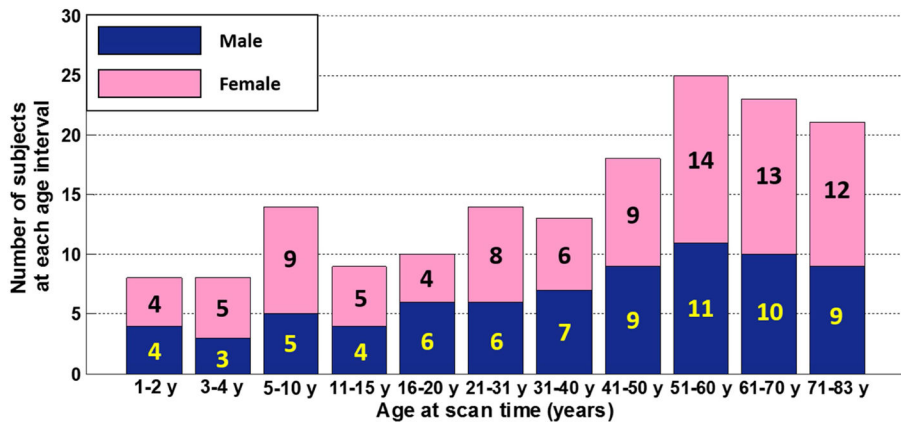
Figure 2.
Number of subjects at each age interval for atlas construction.

Figure 3. Outline of the two-step group-wise registration for longitudinal QSM atlas construction
(a) & (b) For each age-interval, individual QSM(T1w) hybrid images (blue & green hexagons) were combined using Eq. (2) to generate the age-specific atlases (blue & green diamonds). (c) A longitudinal group-wise registration was conducted to generate the longitudinal atlas and compute deformation fields. (d) & (e) the each longitudinal QSM and T1-weighted atlas were finally generated by applying the deformation field to each native individual QSM and T1-weighted images, respectively.

Figure 4. Flow chart for creating longitudinal QSM atlas parcellation map
Step 1: Register T1-weighted atlas from MNI space towards the T1-weighted atlas in the proposed longitudinal atlas space, using affine registration and non-linear registration. Step 2: Apply the deformation field generated during Step 1 on the AAL2 parcellation map and JHU DTI-based white-matter atlas to create cortical parcellation map and white matter parcellation in the proposed longitudinal atlas space. Step3: Draw deep gray matter ROIs using the longitudinal QSM atlas, then combine the DGM ROIs with the cortical & white matter parcellation maps to generate a "whole brain QSM parcellation map".
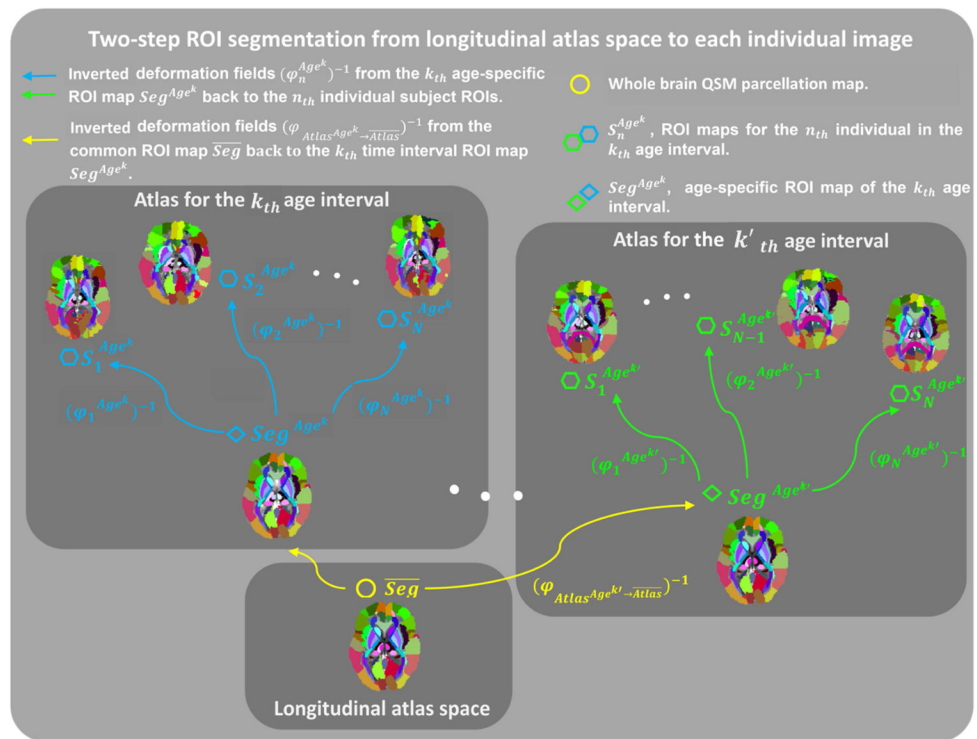
Figure 5. Flow chart for individual QSM image segmentation based on longitudinal QSM atlas parcellation

Based on the longitudinal atlas (the yellow circle), a precise parcellation map is constructed, and is warped back to each age-dependent QSM atlas space. Finally, the ROIs in the individual subjects can be easily synthesized using the inverted deformation fields as described in Eq. (3).
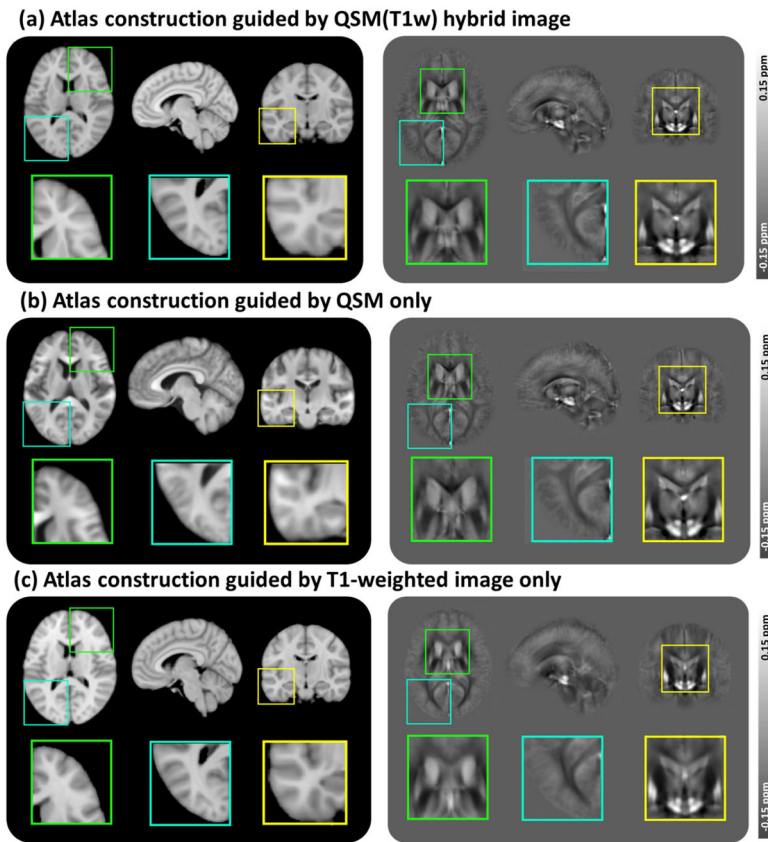
Figure 6. Comparison of the longitudinal atlas construction guided by different contrasts
(a) T1-weighted and QSM atlases guided by QSM(T1w) hybrid contrast as presented in Sec. 1.1.2. (b) T1-weighted and QSM atlases guided by QSM only. (c) T1-weighted and QSM atlases guided by T1-weighted images only. The atlases construction guided by QSM(T1w) hybrid contrast reveal structures more sharply in both cortical region and deep gray matter regions.
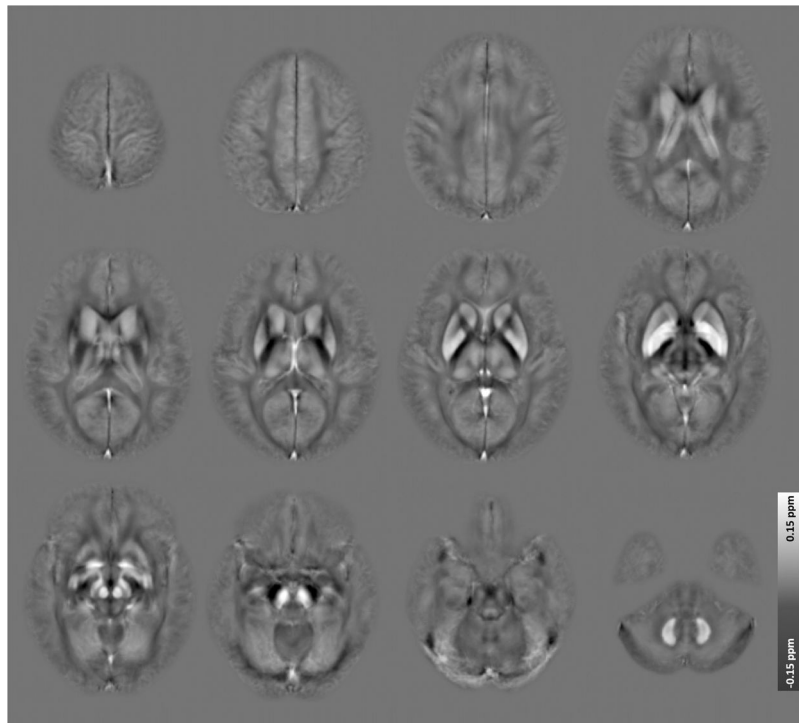
Figure 7.
Construction of the longitudinal atlas from all adult subjects (age 21–83) years using the proposed method.
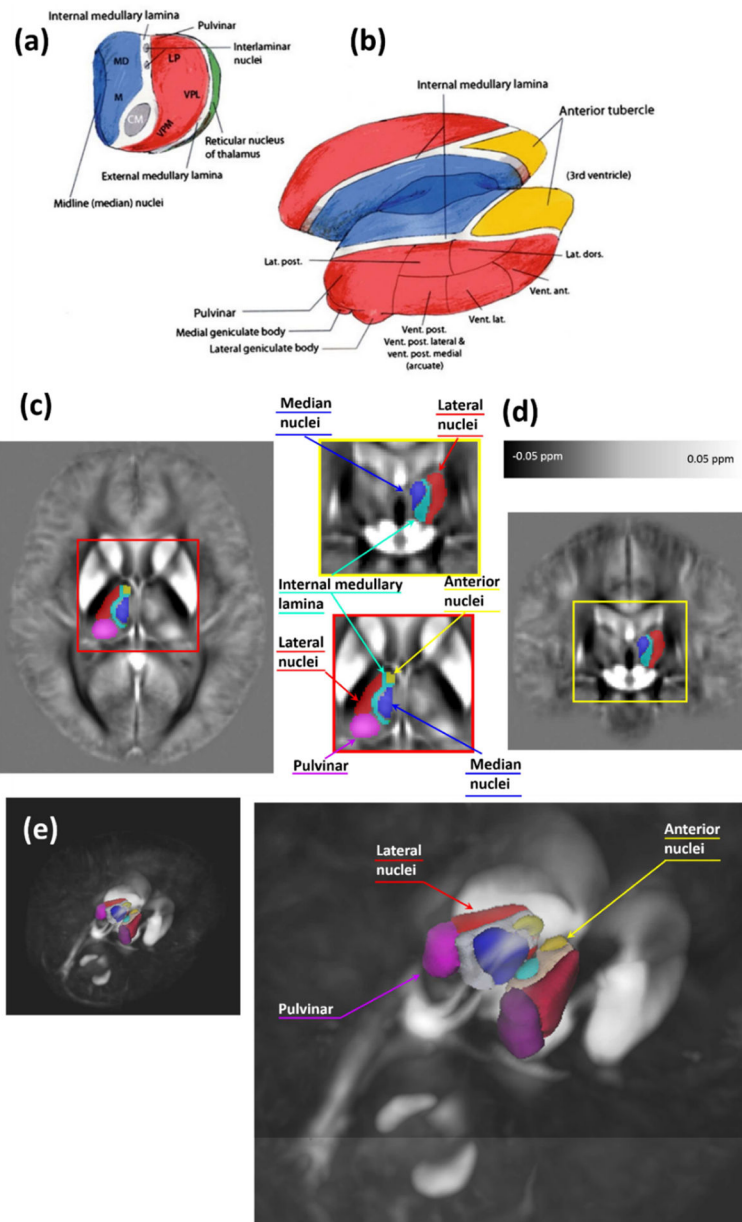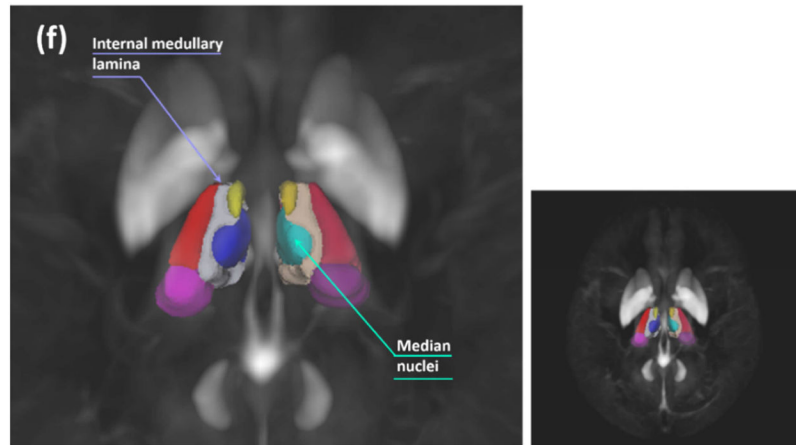
Figure 8. Thalamus parcellation map
(a) Coronal cross-section showing the anatomical structure of a unilateral thalamus. (b) Anatomical structure of bilateral thalamus. (Jacobson and Marcus 2011) (c) Thalamus parcellation map based on the longitudinal QSM atlas in axial view. (d) Thalamus parcellation map based on the longitudinal QSM atlas in coronal view. (e) & (f) 3D rendering of the thalamus parcellation map with the background of the maximum intensity projection of the longitudinal QSM atlas.
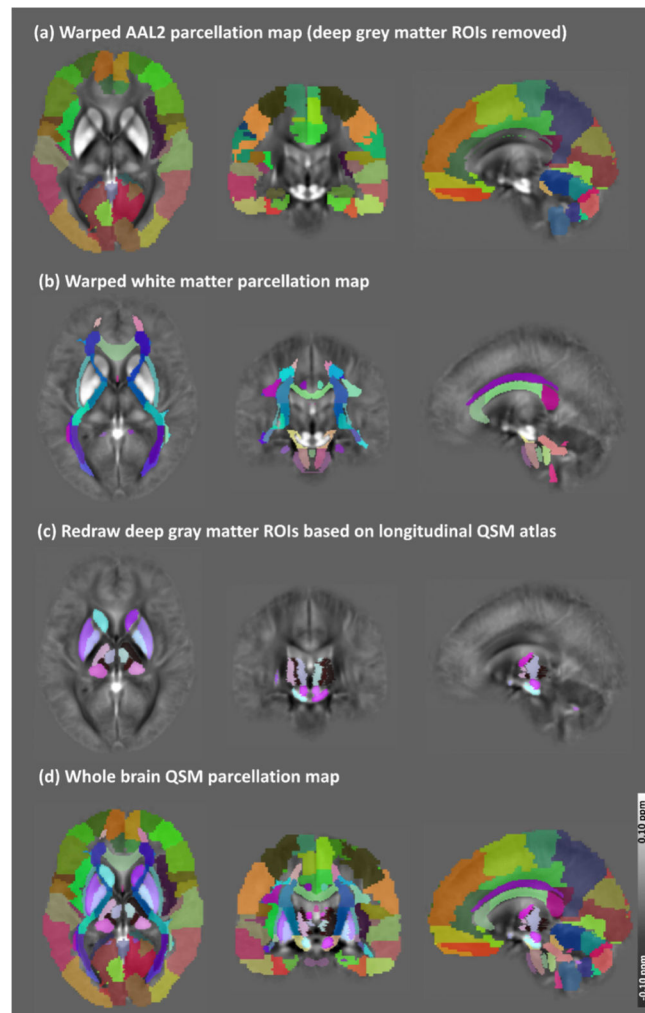
Figure 9. Regions of interest overlaid on QSM images in the axial, sagittal, and coronal planes
(a) The cortical parcellation map propagated from the warped AAL2 atlas. (b) The white matter parcellation map propagated from the warped JHU DTI-based white-matter atlas. (c) The DGM map created using the QSM contrast. (d) The "whole brain QSM parcellation map" formed by combining the warped AAL2 parcellation map, the warped JHU white-matter atlas and the DGM map. In all, 204 ROIs were created for segmenting the whole brain.
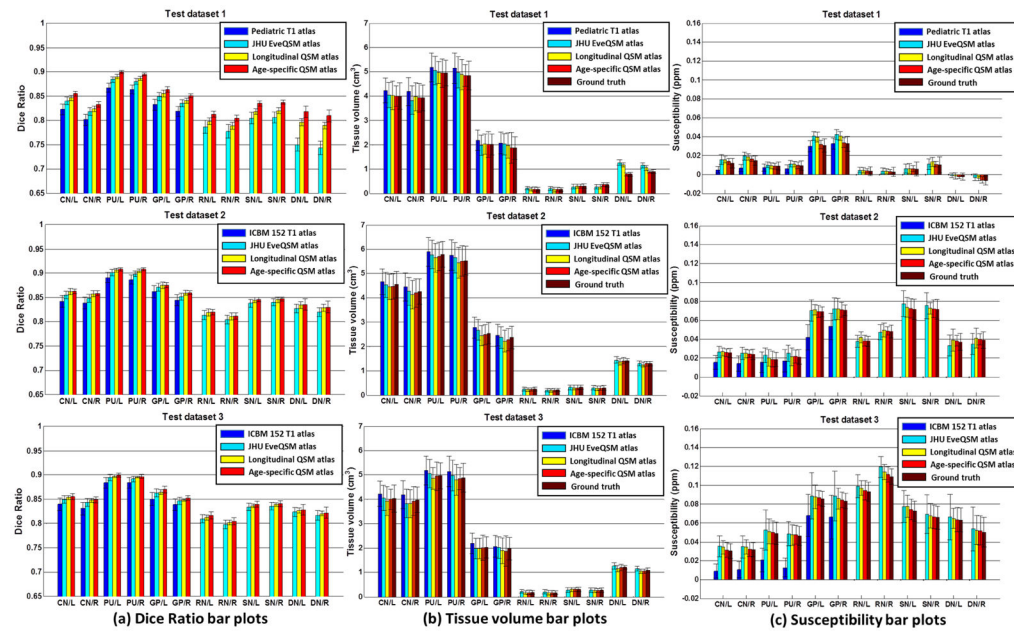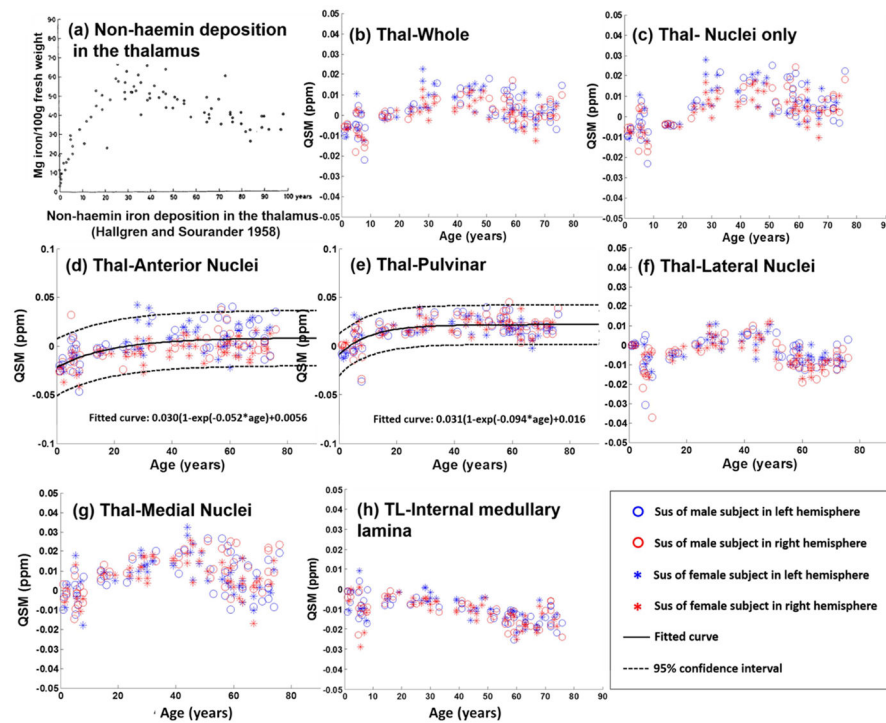
Figure 10.
Bar plots of *(a) dice ratio, (b) tissue volume, (c) mean magnetic susceptibility* in ROIs defined using the Pediatric atlas (Fonov, Evans et al. 2011), the ICBM 152 T1-weighted atlas (Fonov, Evans et al. 2009), the EveQSM atlas (Lim, Faria et al. 2013), the proposed longitudinal atlas, and the proposed age-specific atlas for automatic ROI annotation respectively. The majority voting of the six ROI annotations from three raters, two times labelling, is defined as the ground truth.
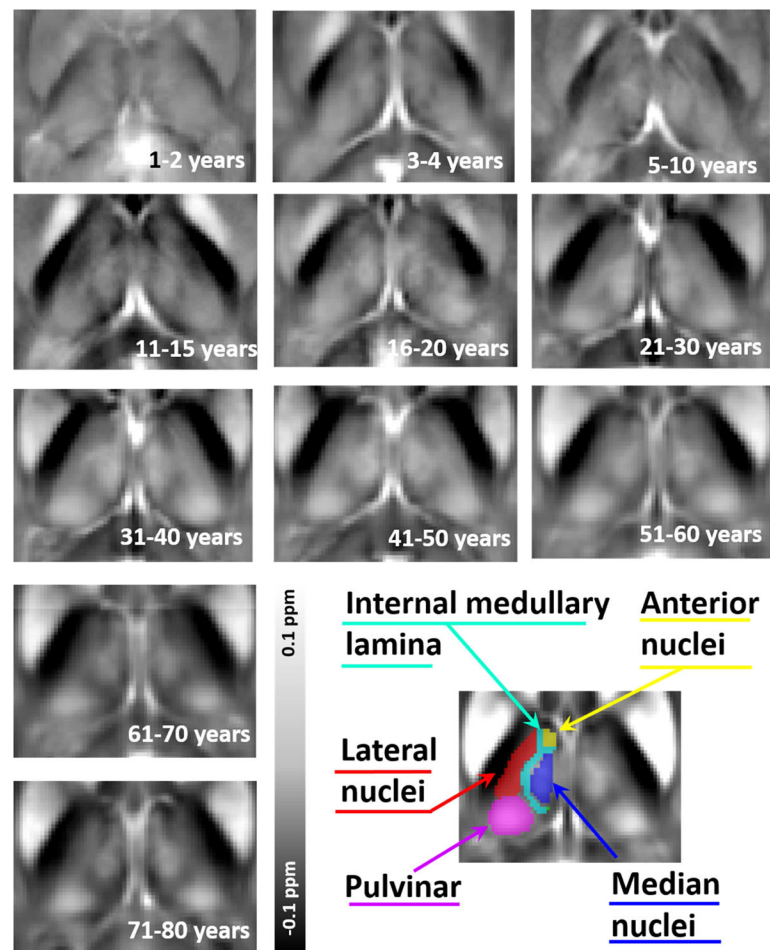
Figure 11. Anatomical development in age-specific susceptibility atlases with aging for the thalamus (Thal)

The magnetic susceptibility developments within the thalamic nuclei vary with aging. The susceptibility of anterior nuclei and pulvinar becomes more paramagnetic with aging; the susceptibility of median nuclei and lateral nuclei firstly increases then decrease with aging; the susceptibility of internal medullary lamina decreases compared to the surrounding tissues. (Due to the different developmental trajectory in different thalamic nuclei (as shown in Fig. 12), the susceptibility contrast within thalamus varied with aging as well, which lead to difficulty in observing absolute susceptibility variation by visual inspection.)

Figure 12. Susceptibility development with age in the Thalamus
(a) Non-haemin iron deposition (Mg Iron/100g fresh tissue weight) development with aging in the thalamus reported by Hallgren and Sourander (Hallgren and Sourander 1958). (b) In the whole thalamus region, the susceptibility development indicates an initial increase from 1–35 years-old and followed by a decrease in the later ages. Sub-figure (c) shows the average susceptibility development in all the thalamic nuclei, the internal medullary lamina is excluded for more accurate iron related estimate. (d) & (e) The Susceptibility in the anterior nuclei and the pulvinar shows consistent growth, and is fitted with the exponential growth pattern in Eq. (5); (f) & (g) the susceptibility in the lateral nuclei and median nuclei shows bidirectional patterns; (h) in the internal medullary mania, the susceptibility decreases with age monotonically.

Table 1

Average Dice Ratios between each segmentation

Dice Ratios (overall average values)			
	Test dataset 1	Test dataset 2	Test dataset 3
Intra-rater (Rater 1)	0.82±0.06	0.86±0.04	0.84±0.04
Intra-rater (Rater 2)	0.83±0.05	0.87±0.03	0.85±0.03
Intra-rater (Rater 3)	0.82±0.06	0.85±0.03	0.86±0.04
Inter-rater (Rater 1&2)	0.82±0.05	0.86±0.04	0.86±0.05
Inter-rater (Rater 1&3)	0.82±0.07	0.86±0.03	0.85±0.03
Inter-rater (Rater 2&3)	0.81±0.07	0.84±0.03	0.84±0.04
Ground Truth vs Rater 1	0.82±0.04	0.86±0.04	0.85±0.03
Ground Truth vs Rater 2	0.83±0.05	0.85±0.03	0.86±0.04
Ground Truth vs Rater 3	0.81±0.04	0.87±0.02	0.85±0.03
Ground Truth vs. Automated segmentation (using age-specific QSM atlases)	0.81±0.06	0.86±0.03	0.85±0.04

Table 2

The fitted model of susceptibility in brain nuclei.

Putamen	$Sus[ppm] = 0.078(1 - exp(-0.023 * age[y/o])) - 0.015$
Caudate nucleus	$Sus[ppm] = 0.032(1 - exp(-0.039 * age[y/o])) + 0.0054$
Globus pallidus	$Sus[ppm] = 0.086(1 - exp(-0.049 * age[y/o])) + 0.017$
Substantia nigra	$Sus[ppm] = 0.12(1 - exp(-0.028 * age[y/o])) - 0.0052$
Red nucleus	$Sus[ppm] = 0.10(1 - exp(-0.044 * age[y/o])) - 0.011$
Dentate nucleus	$Sus[ppm] = 0.0090(1 - exp(-0.043 * age[y/o])) - 0.032$
Amygdala	$Sus[ppm] = 0.040(1 - exp(-0.069 * age[y/o])) - 0.030$
Hippocampus	$Sus[ppm] = 0.020(1 - exp(-0.032 * age[y/o])) - 0.0012$
Anterior nucleus of thalamus	$Sus[ppm] = 0.0030(1 - exp(-0.052 * age[y/o])) + 0.0056$
Medial nucleus of thalamus	$Sus[ppm] = 0.018(1 - exp(-0.11 * age[y/o])) - 0.015$
Pulvinar of thalamus	$Sus[ppm] = 0.031(1 - exp(-0.094 * age[y/o])) - 0.016$